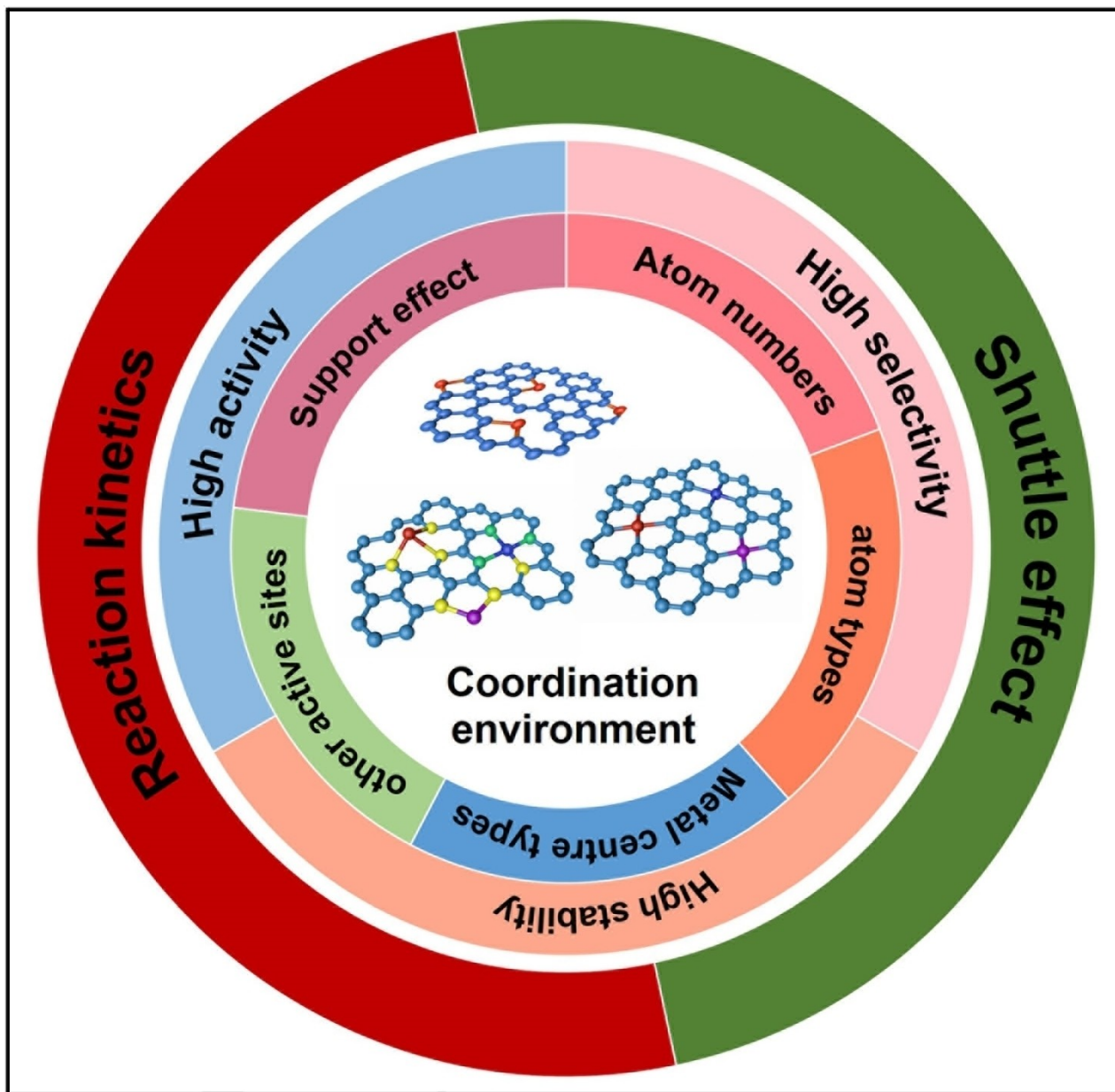


# Coordination Manipulation of Single Atom Catalysts for Lithium-Sulfur Batteries: Advances and Prospects

Haorui Zhao,<sup>[a]</sup> Yingze Song,<sup>\*[b]</sup> and Jingyu Sun<sup>\*[a]</sup>



On account of high energy density and low cost of sulfur, lithium-sulfur (Li–S) battery has been regarded as an appealing energy storage system to date. Nevertheless, it has faced formidable challenges, mainly pertaining to the fatal shuttle effect and retarded sulfur redox kinetics. Single atom catalysts (SACs) have showcased great promise for addressing these issues owing to their maximum atom utilization efficiency, favorable catalytic activity as well as their good structural tunability at an atomic level, considerably contributing to the

recent fruitful advancements in Li–S realm. In this review, we summarize the state-of-the-art strategies in the coordination manipulations of SACs toward highly efficient and durable Li–S batteries. The recent advances, existing issues, and future outlooks are discussed accordingly, aiming to guide the synthetic design of SACs, propel the underlying mechanism understanding and ultimately boost the commercial viability of Li–S batteries.

## 1. Introduction

As an emerging energy storage system, lithium-sulfur (Li–S) batteries are deemed as one of the most appealing rechargeable battery systems owing to the multi-electron transfer feature in sulfur redox reaction. Along this line, Li–S batteries attain high theoretical specific capacity (1675 mAh g<sup>-1</sup>) and gravimetric energy density (2600 Wh kg<sup>-1</sup>).<sup>[1]</sup> In addition, the environmental friendliness and low cost of sulfur drive more feasibility of Li–S batteries in the aspect of practical applications,<sup>[2]</sup> thus leading to tremendous attention in energy storage realm. Unfortunately, notorious “shuttle effect” and sluggish sulfur redox kinetics result in the irreversible loss of sulfur, lithium anode corrosion as well as the incomplete discharge process, further causing inferior capacity and short cycling lifespan of Li–S batteries.<sup>[3,4]</sup> Various materials with micrometer or nanometer sizes, mainly involving metal oxides/carbides/sulfides/brides/phosphides, etc.,<sup>[5–11]</sup> have been fabricated as adsorptive and/or catalytic mediators to address above obstacles. Despite fruitful progresses thus far, it is still urgently desired to develop novel catalysts with higher activity for optimizing the Li–S redox reactions.<sup>[12]</sup> Additionally, it is worth-noting that the metal compound-based catalysts usually increase the weight of electrode, which produces adverse effect on the gravimetric energy density of batteries.<sup>[13–15]</sup> In view of this, it is of utmost significance to exploit advanced alternatives with high catalytic activity and light weight to manipulate the procedures of Li<sub>2</sub>S precipitation and decomposition.

It's evident that the activity of catalysts can be increased by decreasing their sizes.<sup>[16]</sup> In this regard, Pt single atom catalyst (SAC) was firstly proposed in 2011 by Zhang et al. to promote the CO oxidation.<sup>[17]</sup> With the aid of isolated Pt atoms, the

related energy barriers were effectively reduced, hence accelerating the CO oxidation reaction kinetics. Upon persistent efforts, recently developed SACs have readily exhibited conspicuous activity and consequently become one of the most encouraging frontiers in the field of energy conversion. Integrating merits of both heterogeneous and homogenous catalysts,<sup>[12]</sup> SACs with well dispersed metal atoms on appropriate supports harness high selectivity, activity, stability for electrochemical applications.<sup>[18–20]</sup> Compared with bulk and nanosized catalysts,<sup>[21,22]</sup> isolated metal atoms expose on the surface of substrates, offering opportunities to contact with the reactive species, which would result in maximum atom utilization efficiency.<sup>[23]</sup> Moreover, the metal centers are activated due to the different local coordination environments, and thus present high selectivity during the reaction pathways.<sup>[24–26]</sup> SACs might also ensure high stability via strong chemical interaction or charge transfer between metal atoms and supports.<sup>[27,28]</sup> Of note, the geometric and electronic structures of SACs can be easily tuned by coordination engineering, fulfilling the higher activity, selectivity as well as stability in contrast to the metal compound catalysts. Owing to these collective merits, SACs have been widely applied in catalysis fields including hydrogen evolution reaction,<sup>[29–31]</sup> oxygen reduction reaction,<sup>[32–36]</sup> carbon dioxide reduction reaction,<sup>[37,38]</sup> and nitrogen reduction reaction.<sup>[39–41]</sup> More recently, SACs have become preferable catalytic candidates in Li–S battery systems,<sup>[42–44]</sup> providing new chances to the optimization of Li–S redox reaction efficiency and the final battery performance. Along this line, modulating coordination configurations and uncovering the intrinsic mechanism of SACs in Li–S chemistry is essential and significant.

To date, there have been some significant review articles summarizing the applications of SACs in Li–S batteries.<sup>[45–47]</sup> Nevertheless, in-depth discussions on coordination modulation of SACs in Li–S realm are rarely carried out. In this sense, a comprehensive summary of the recent advances in the coordination-modulated SACs in Li–S battery systems would be highly desirable. In this review, we aim at providing valuable insights into the rational coordination modulation for attaining SACs toward boosted Li–S electrochemistry. To begin with, we introduce the concepts of bidirectional Li–S catalysis process. We then summarize the existing strategies of modulating local coordination environments of SACs, encompassing coordination atom number, non-metal atom center type, metal atom type, supports and integration with other active centers (Fig-

- [a] H. Zhao, Prof. J. Sun  
College of Energy  
Soochow Institute for Energy and Materials Innovations  
Key Laboratory of Advanced Carbon Materials and Wearable Energy  
Technologies of Jiangsu Province  
Soochow University  
Suzhou 215006 (P.R. China)  
E-mail: sunjy86@suda.edu.cn
- [b] Y. Song  
State Key Laboratory of Environment-Friendly Energy Materials  
Tianfu Institute of Research and Innovation, School of Materials and  
Chemistry  
Southwest University of Science and Technology  
Mianyang 621010 (P.R. China)  
E-mail: yzsong@swust.edu.cn

ure 1). Meanwhile, the catalytic mechanisms are also deciphered to shed light on the performance enhancement in Li–S systems. Finally, we propose future perspectives for the reliable development of SACs targeting high-performance Li–S batteries.

## 2. Fundamentals in Li–S batteries

### 2.1. Bidirectional sulfur electrochemistry

A typical Li–S battery acts as a rechargeable energy storage system, incorporating sulfur cathode, Li metal anode, electrolyte and separator.<sup>[48]</sup> Different from the intercalation-type mechanism of lithium-ion batteries,<sup>[49]</sup> Li–S batteries possess more favorable specific capacity and energy density, which heavily depends on the multi-electron reactions.<sup>[50]</sup> Throughout the breakage and regeneration of S–S bonds, chemical energy effectively transforms to electrical energy in Li–S systems. In general, such a chemistry process refers to the specific reaction:  $S_8 + 16Li^+ + 16e^- \leftrightarrow 8Li_2S$ .<sup>[51]</sup> Multi-phase pathways occur during sulfur reduction reaction (SRR), pertaining to the stepwise conversion of solid to liquid phase ( $S_8 \rightarrow Li_2S_8$ ) at 2.8 V, liquid to liquid phase ( $Li_2S_8 \rightarrow Li_2S_x$ ,  $4 \leq x \leq 6$ ) at approximately 2.4 V, and liquid to solid phase ( $Li_2S_x \rightarrow Li_2S_2/Li_2S$ ,  $4 \leq x \leq 6$ ) at 2.1 V, corresponding to the two typical plateaus in the discharge/charge curve of Li–S batteries. It's noted that the reduction reaction ends up with the final formation of  $Li_2S$  product at 1.7 V.<sup>[52]</sup> In terms of the charge procedure,  $Li_2S$  is decomposed and accordingly returns to the initial state of  $S_8$  by experiencing the sulfur oxidation reaction (SOR). Such a bidirectional sulfur evolution process contributes to the discharge and charge capacities.

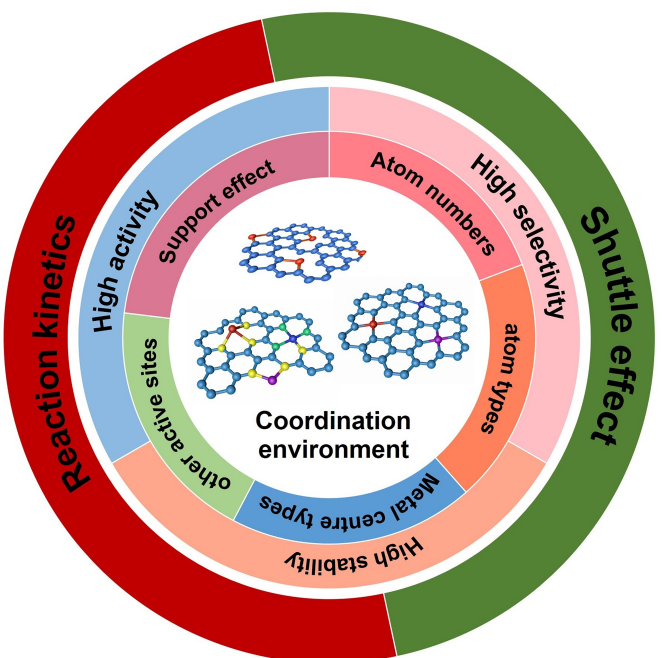


Figure 1. Schematic diagram of coordination modulation of SACs for efficient Li–S system.

### 2.2. Challenges in Li–S batteries

Notwithstanding the fact that Li–S batteries exhibit outstanding theoretical capacity and energy density, fatal problems still need to be tackled to promote its practical development. Thus far, a number of functional additives have been used to optimize the sulfur cathode.<sup>[53]</sup> Nonetheless, the high weight of introduced component materials might lower the practical energy density of overall Li–S cells. In addition, the density differences between sulfur ( $2.06 \text{ g cm}^{-3}$ ) and  $Li_2S$  ( $1.66 \text{ g cm}^{-3}$ ) give rise to a large volume variation during the discharge and charge process,<sup>[19,54]</sup> leading to the cracks and collapses



Haorui Zhao is pursuing her Master's degree under the supervision of Prof. Jingyu Sun in College of Energy, Soochow Institute for Energy and Materials Innovations, Soochow University. Her current research interests focus on the suitable manipulation of single atom catalysts for high-performance Li–S batteries.



Yingze Song obtained his Ph.D. from Soochow University in 2019 under the supervision of Prof. Jingyu Sun and Prof. Zhongfan Liu. During 2013–2015, he worked in Ningbo Institute of Materials Technology & Engineering, CAS. Since July 2019, he became a full professor in State Key Laboratory for Environment-Friendly Energy Materials, Southwest University of Science and Technology. His current research interests deal with emerging materials for efficient energy storage.



Jingyu Sun earned his bachelor's degree from Zhejiang University in 2008 and obtained his Ph.D. from University of Oxford in 2013. After postdoc training at Peking University and University of Cambridge, he became a full professor in College of Energy, Soochow University in 2017. His research interests focus on chemical vapor deposition design of graphene-based materials and advanced printing methodology for energy devices.

occurred within the cathode upon long-term cycling. Another key problem existing in Li–S batteries involves of notorious shuttle effect and slow sulfur redox kinetics. Long-chain lithium polysulfides (LiPSs) are prone to dissolve in electrolyte and then diffuse to the Li metal anode side. Subsequently, parts of LiPSs return to cathode owing to the effects of concentration gradient and electric field, which is denoted as “shuttle effect”. Such a shuttle phenomenon results in the severe self-discharge, low Coulombic efficiency, and rapid capacity decay. Meanwhile, the retarded sulfur conversion kinetics result from the following aspects: i) the electron conductivities of  $S_8$  molecule and  $Li_2S$  product are only  $5 \times 10^{-30}$  and  $3.6 \times 10^{-7} \text{ S cm}^{-1}$ , respectively,<sup>[55]</sup> which yield large diffusion resistances; ii) the high energy barriers occurred in SOR and SRR are difficult to be surmounted; iii) the accumulated  $Li_2S$  on the surface of Li anode is also responsible for the sluggish redox kinetics; iv) the viscosity change originating from the sulfur evolution could also affect the reaction kinetics to a certain extent; v) the solid ( $Li_2S_2$ )-solid ( $Li_2S$ ) phase conversion can slow down the electrochemical reaction. The sluggish reaction kinetics indeed poses a large threat to the holistic electrochemical performances of Li–S batteries.

Upon strenuous efforts, fruitful progresses have been gained in addressing these issues. Nevertheless, there still existing intractable challenges wait to be tackled. In the past decades, physical and chemical adsorptive mediators were applied to mitigate the shuttle effect. To date, various mediators with the electrocatalytic function have been explored to accelerate the generation and decomposition of  $Li_2S$  in the discharge and charge procedure, respectively.<sup>[56,57]</sup> Unfortunately, most of them normally show limited activity and unidentified catalysis impact on the stepwise conversion of  $S_8$  to  $Li_2S$ . The rational design of electrocatalysts toward the simultaneous kinetics acceleration in reduction and oxidation process is urgent to be carried out. In this respect, the size manipulation-enabled SACs have emerged as an advanced enabler to boost the electrocatalytic activity of mediators in sulfur electrochemistry.

### 3. Coordination Modulation Strategies

It's meaningful for electrocatalysts to pursue smaller size instead of larger chunk toward markedly increased catalytic activity. With the exposed isolated metal atoms on the surface of supports, SACs harness maximized atom utilization, enhanced LiPS binding strength and catalytic activity, hence improving the battery performance.<sup>[58]</sup> Throughout the modulation of coordination environment, metal centers can be activated owing to the upshifts in *d* band, causing that density of states are closer to the Fermi level and electrons are easier to fill the orbitals, giving rise to the hybridizations of metallic and non-metallic *s-p* orbitals.<sup>[59,60]</sup> According to the Lewis acid-base theory, metal centers are in favor of binding with S species, rendering stronger adsorption. In addition, tuning the coordination environment can enrich the types of SACs,<sup>[61,62]</sup> which is conducive to the design of efficient electrocatalysts for

Li–S batteries. To better explore the modulated dispersion and structure of SACs, a wealth of advanced characterizations involving high-angle annular dark-field scanning transmission electron microscopy (HAADF-STEM)<sup>[63–65]</sup>, X-ray absorption near-edge structure (XANES),<sup>[66,67]</sup> extended X-ray absorption fine structure (EXAFS),<sup>[68]</sup> and time-of-flight secondary ion mass spectrometry (TOF-SIMS)<sup>[69]</sup> have been employed. With the aid of these toolsets, the types and functions of SACs toward the sulfur evolution can be clearly disclosed.

#### 3.1. Coordinated atom number

The coordinated atom number serves as the key factor for the structural stability and electrocatalytic activity of SACs. In metal–N–C (M–N–C) moieties, the coordination form of M–N<sub>4</sub> shows bidirectional catalytic capability for the  $Li_2S$  nucleation and decomposition. Du *et al.*<sup>[43]</sup> reported a Co–N<sub>4</sub> catalyst in the cathode along with 90 wt.% sulfur content could facilitate the bidirectional redox reaction. To date, the explorations of M–N<sub>4</sub> coordinated SACs have eventually become mature in Li–S system. Zhao *et al.*<sup>[70]</sup> designed a self-standing sulfur host with the addition of Fe single atom loading on porous carbon nanofibers. It is worth-mentioning that the active Fe moieties surrounded with graphitic N to form the Fe–N<sub>4</sub> coordination could effectively optimize the electrochemical reaction. The above results show that configuration pertaining to the four N atoms endows the SACs with excellent catalytic ability. Li *et al.*<sup>[67]</sup> designed an active Ru-SAC-incorporated Janus separator by the interfacial engineering strategy. They proved that faster SOR process occurs at Ru-SAC than bare reduced graphene oxide (rGO) (Figure 2a). During the transition from  $Li_2S_8$  to  $Li_2S$ , it can be seen from Figure 2(b) that the energy barrier increases under the reaction process, corresponding to more difficult reduction. However, the single Ru atoms can significantly reduce the activation energy ( $E_a$ ) in contrast to the rGO, indicative of faster  $Li_2S$  nucleation reaction. The great current response and small voltage polarization from the cyclic voltammogram (CV) test further demonstrate its outstanding redox reaction kinetics (Figure 2c). Meanwhile, the multifunctional separator with the Janus structure could not only inhibit the LiPS shuttling but also enhance the Li-ion flux toward the suppressed lithium dendrite growth.

Aside from the saturated M–N<sub>4</sub> form, M–N–C catalysts with other N coordinated numbers rather than four have also been reported to propel the sulfur redox reactions. Wang *et al.*<sup>[71]</sup> designed SACs with a low coordination number Fe–N<sub>2</sub> (Fe–N<sub>2</sub>–NC) to draw a comparison of the catalytic impact difference between the Fe–N<sub>2</sub> and Fe–N<sub>4</sub> configurations. According to the density functional theory (DFT) results, it was firstly confirmed that the Fe–N<sub>2</sub> configuration respectively owned larger electron density and higher *d* band centers than those of Fe–N<sub>4</sub>. It showed that more metallic properties in Fe–N<sub>2</sub> exhibited more considerable distributions around the Fermi level. With the stronger hybridization of Fe 3d<sub>z</sub> and S 3p<sub>y</sub> orbitals, the higher trapping ability for long-chain LiPSs is realized (Figure 2d). Linear scanning voltammetry (LSV) curves

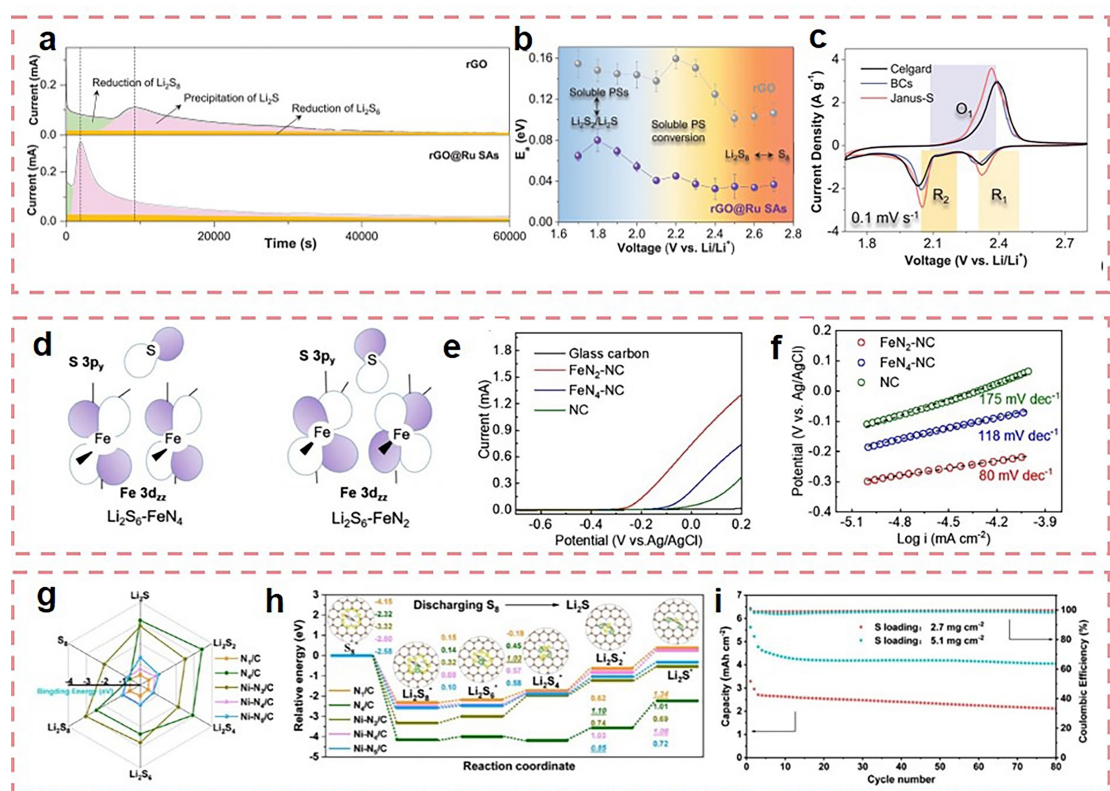


**Figure 2.** a) Potentiostatic discharge profiles of the rGO and rGO@Ru SAs electrodes. b)  $E_a$  profiles of the rGO and rGO@Ru electrodes at different voltages. c) CV curves of the Li–S batteries based on Celgard, BCs and Janus-S separator. Reproduced with permission from Ref. [67]. Copyright (2021) Wiley-VCH. d) The interaction orbital diagram of  $\text{Li}_2\text{S}_6\text{-FeN}_4$  and  $\text{Li}_2\text{S}_6\text{-FeN}_2$ . e) LSV curves and the corresponding f) Tafel curves of  $\text{FeN}_2\text{-NC}$ ,  $\text{FeN}_4\text{-NC}$  and NC. Reproduced with permission from Ref. [71]. Copyright (2022) Elsevier. g) Binding energies of LiPSs on the five catalyst models. h) Energy profiles for the discharge process of  $\text{S}_8$  to  $\text{Li}_2\text{S}$  on the five catalyst models. Inset images are the optimized structures of LiPSs adsorption configurations on  $\text{Ni}-\text{N}_5/\text{C}$ . i) Cycling performance of  $\text{Ni}-\text{N}_x/\text{HPNC/S}$  cathodes with S areal loading of 2.7 and 5.1 mg cm<sup>-2</sup>, respectively. Reproduced with permission from Ref. [74]. Copyright (2021) American Chemical Society.

manifest the smaller energy barrier for  $\text{Li}_2\text{S}$  decomposition over  $\text{Fe}-\text{N}_2$  in contrast to  $\text{Fe}-\text{N}_4$  (Figure 2e). In the reverse process, the faster redox reaction current response and larger integral area substantiated the superior capability of  $\text{Fe}-\text{N}_2\text{-NC}$  in inducing the  $\text{Li}_2\text{S}$  nucleation. Such results are also verified by the Tafel slope plots in Figure 2(f). Fang *et al.*<sup>[72]</sup> proposed an exfoliation-evaporation strategy that enabled the Co-SACs with different N coordination numbers. Throughout the experimental operations and theoretical calculations, they revealed that Co–N<sub>2</sub> with asymmetric electron distribution could showcase outstanding ability in immobilizing LiPSs and promoting  $\text{Li}_2\text{S}$  deposition/dissociation compared to the Co–N<sub>4</sub> configuration. As a result, a high capacity of 687 mAh g<sup>-1</sup> at 5 C was attained, demonstrating that unsaturated structure might be in favor of boosting the sulfur redox kinetics.

Along with the unsaturated M–N<sub>2</sub> configuration, the over-saturated M–N<sub>5</sub> form has also attracted considerable research interests. Zhang *et al.*<sup>[73]</sup> synthesized SACs with an over-saturated Fe–N<sub>5</sub> coordination by an adsorption-pyrolysis procedure. They confirmed that the Fe–N<sub>5</sub> coordination could effectively alleviate the shuttle effect and catalyze the electrochemical reaction, providing a comprehensive understanding in the effect of over-saturated coordination on the catalytic activity. Wang's group<sup>[74]</sup> reported an over-saturated SAC consisted of an

isolated Ni atom in hollow N-doped porous carbon, realizing the coordination of single Ni metal center with different numbers of N atoms ( $\text{Ni}-\text{N}_x$ ,  $x=3\text{--}5$ ). As displayed in Figure 2(g and h), the catalysts obtain the smallest Gibbs energies during discharge process from  $\text{S}_8$  to  $\text{Li}_2\text{S}$ . The lowest energy barrier usually implies the rate-limiting step in the whole sulfur conversion process. It was found that the  $\text{Ni}-\text{N}_5/\text{C}$  obtained the most favorable reaction thermodynamics among the samples. As the candidate cathodes, the S/Ni–N<sub>5</sub>/HPNC exhibited a superior specific capacity at high rates and a lower decay over long cycling. When the sulfur loading was up to larger value, it could still maintain a considerable areal capacity after cycling. These findings reveal that the control of coordinated atom number can fulfill the electrocatalytic activity operation to tackle LiPS shuttling, accompanied by the efficient sulfur reaction kinetics.

### 3.2. Non-metallic atom types

Besides the afore-mentioned N atoms, other non-metallic heteroatoms including O, S, P, etc.<sup>[75,76]</sup> are also introduced to participate the coordination design. For instance, Li *et al.*<sup>[23]</sup> reported a separator modified by Co–O<sub>4</sub> moieties, with "single

atom array mimic" on ultrathin metal organic framework (MOF) nanosheets for attaining long-life Li–S batteries. The abundant exposed O atoms effectively anchored LiPSs by strong Lewis acid interaction with Li atoms. Noting that the coordination of single metal atom with two types of non-metallic atoms has become a new fashion to design the electrocatalytic activity of SACs. Generally, the introduction of dual heteroatoms into the supports is the critical step for performing the dual coordination modulation. For example, Liu *et al.*<sup>[77]</sup> selected N and O-rich carbon framework as the support to fulfill the dual coordination of Mn atom with N and O atoms. The synergy of dual coordination environments can be beneficial to anchoring LiPSs and accelerating the LiPS conversion kinetics. In another work, Wang *et al.*<sup>[78]</sup> fabricated a unique W–O<sub>2</sub>N<sub>2</sub>–C catalyst to optimize Li–S systems. Such a local atomic structure tailoring remarkably propels the Li<sub>2</sub>S decomposition on W–O<sub>2</sub>N<sub>2</sub>–C by reducing the reaction energy barriers.

P atoms are also employed to assist the realization of such dual coordination toward efficient electrochemical reaction. Huang *et al.*<sup>[79]</sup> devised an efficient polymerization-carboniza-

tion strategy to fabricate N, P coordinated Fe single atoms for Li–S batteries. Figure 3a and b demonstrate that N and P atoms are successfully coordinated with single metal Fe moieties. Potentiostatic discharge tests exhibit the earlier peak current response and more Li<sub>2</sub>S precipitation on FeSA–PN@PNC than FeSA–N<sub>x</sub>@PNC (Figure 3d). The SEM insets further reveal the uniform distributions of Li<sub>2</sub>S on the FeSA–PN@PNC surface, confirming the promoted sulfur conversion reaction kinetics. In addition, the lower energy barrier of Li<sub>2</sub>S on FeSA–PN@PNC substantiates the boosted reaction kinetics of charge procedure (Figure 3c). With the signals orderly declined up to thoroughly vanished in discharge process and reversely regenerated in charge process, *operando* Raman measurement further revealed the underlying mechanism of dual coordination-enabled LiPS evolution.

The adsorption property and catalytic ability of SACs are influenced by the orbital hybridization originating from the *d* orbitals of metal and *p* orbitals of sulfur species. SACs always form  $\sigma$  and  $\pi$  bonds based on the  $d_z^2$  of metal with  $p_z$  of sulfur and the  $d_{xz/yz}$  of metal with  $p_{xy}$  of sulfur, respectively. Liu *et al.*<sup>[80]</sup>

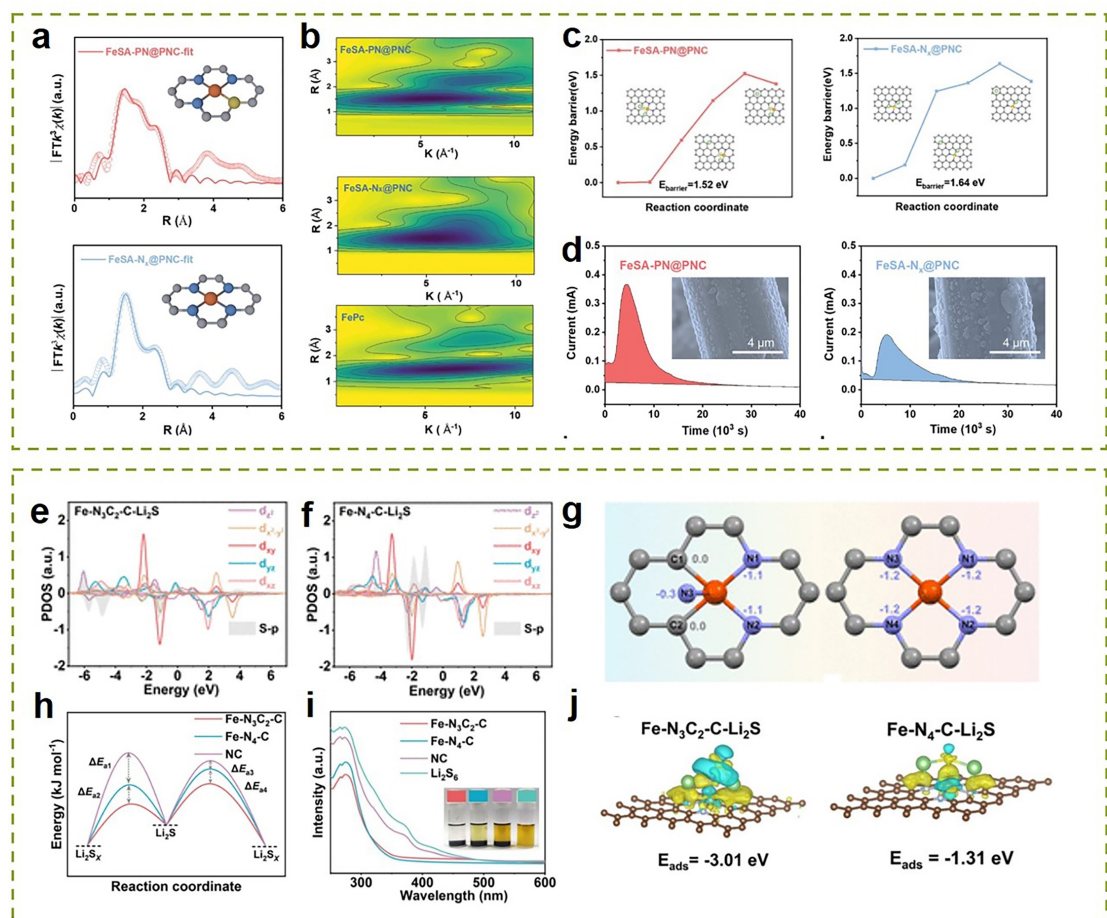


**Figure 3.** a) EXAFS fitting curves of FeSA–PN@PNC and FeSA–N<sub>x</sub>@PNC. b) Wavelet transforms for FeSA–PN@PNC, FeSA–N<sub>x</sub>@PNC, and FePc. c) The decomposition energy barriers of Li<sub>2</sub>S on FeSA–PN@PNC and FeSA–N<sub>x</sub>@PNC. d) Potentiostatic discharge profiles at 2.05 V for the FeSA–PN@PNC, FeSA–N<sub>x</sub>@PNC. Reproduced with permission from Ref. [79]. Copyright (2022) Wiley-VCH. e, f) PDOS of Fe and S. g) Charge density differences of Fe–N<sub>3</sub>C<sub>2</sub>–C–Li<sub>2</sub>S and Fe–N<sub>4</sub>–C–Li<sub>2</sub>S. h)  $E_a$  of the precipitation and decomposition of Li<sub>2</sub>S. i) UV-vis spectra of Li<sub>2</sub>S<sub>6</sub> solutions with different samples. The inset is the digital image of the solutions after adsorbing for 6 h. j) Bader charge numbers of coordination atoms of Fe–N<sub>3</sub>C<sub>2</sub>–C and Fe–N<sub>4</sub>–C. Reproduced with permission from Ref. [80]. Copyright (2022) American Chemical Society.

found that the extra  $\pi$  bond resulted from the hybridization between  $d_{x^2-y^2}$  and  $p$  orbitals through a precisely designed asymmetric coordination configuration. This extra  $\pi$  bond enhanced the chemical affinity with LiPSs. From Figure 3(e and f), both the Fe–N<sub>3</sub>C<sub>2</sub>–C and Fe–N<sub>4</sub>–C form  $\sigma^-$  and  $\pi$  bond stemming from the overlap in  $d_z^2$  and  $d_{xz/yz}$  orbitals of Fe and  $p$  orbitals of sulfur. However, the extra  $\pi$  bond only generates in Fe–N<sub>3</sub>C<sub>2</sub>–C moiety, leading to the superior ability for optimizing sulfur evolution than Fe–N<sub>4</sub>–C configuration. Figure 3(g) shows that the four N atoms are symmetrically distributed around the metal center, resulting in the equal bonding length and bonding energy. However, as for the Fe–N<sub>3</sub>C<sub>2</sub>–C, the asymmetrically distributed configuration caused the different bond length and bond energy. The redistribution of charge density activated  $d_{x^2-y^2}$  and  $d_{xy}$  orbits, formed the extra  $\pi$  bond and enhanced the  $d$ – $p$  orbit hybridization, which greatly promoted the interface electron transfer and hence accelerated sulfur redox reaction. Figure 3(h) shows the smallest  $E_a$  values of Fe–N<sub>3</sub>C<sub>2</sub>–C for the whole redox reaction, further verifying its enhanced catalytic activity. As shown in Figure 3(i), the Fe–N<sub>3</sub>C<sub>2</sub>–C presents the largest intensity descending in UV-vis spectra, and an obvious Li<sub>2</sub>S<sub>6</sub> color fading than other samples, demonstrating its strong LiPS adsorption ability. Charge density images show the more intensive charge transfer in Fe–N<sub>3</sub>C<sub>2</sub>–C, and higher binding energy with Li<sub>2</sub>S (Figure 3j), manifesting that its asymmetric configuration can effectively speed up the sulfur conversion reaction procedure.

### 3.3. Metal center type

Metal center type acts as another key factor of affecting the activity of SACs for Li–S chemistry. Therefore, it is of great significance to seek more favorable metal centers for forming the ideal coordination. Recently have witnessed some progresses in detecting the effect of metal center type on the activity of SACs.<sup>[25,81,82]</sup> In this regard, we reported a class of MN<sub>4</sub>C<sub>4</sub> moieties (Fe, Co, Ni) via a universal synthesis route.<sup>[83]</sup> Through electrochemical measurement and *operando* spectrum probing, Ni-SAC enabled the most favorable catalytic activity for the sulfur conversion in discharge/charge procedures. In detail, theory analysis was employed to depict the catalytic properties and underlying mechanism based on the different metal centers. As shown in Figure 4(a), optimal adsorption models of LiS\* demonstrate the catalytic capability of the active sites in slowest solid-solid reaction stage. The four possible adsorption sites were regarded as the metal center (M), N atom (N), and two carbon sites adjacent to the N atom, which were marked as five-membered ring (C<sub>5</sub>)/six-membered ring (C<sub>6</sub>). According to the calculated Gibbs free energy, the trend of adsorption strength at different sites was: M > C<sub>5</sub> > C<sub>6</sub>. As for M–N<sub>4</sub> moieties, the binding strength of LiS\* followed the order of Fe > Co > Ni. There were two steps in Li<sub>2</sub>S<sub>2</sub> transformation process, which could be listed as follows: i) 3DOL + Li<sub>2</sub>S<sub>2</sub> + Li<sup>+</sup> + e<sup>-</sup> + \* → 3DOL-LiS\* + Li<sub>2</sub>S; ii) 3DOL-LiS\* + Li<sup>+</sup> + e<sup>-</sup> + \* → 3DOL + Li<sub>2</sub>S + \*. Inspired by this, a volcano plot was designed to explain the relation between free energy of LiS\* and negative over-

potential ( $\eta$ ), which were used as the specific thermodynamic descriptors to describe the enhanced optimization ability (Figure 4b). Bader charge analysis in Figure 4(c) shows that M, C<sub>5</sub>, and C<sub>6</sub> sites have positive charges, and the value decreases in the order of M > C<sub>5</sub> > C<sub>6</sub>. Owing to the negative charges of S, it was easier to generate bond interaction under more positive charges, corresponding to the adsorption energy. In view of this, Fe–N<sub>4</sub> displayed the strongest binding energy with LiS\* among the three SACs. Too strong adsorption energy might exhibit an adverse effect on the catalytic capacity otherwise. On the contrary, Ni–N<sub>4</sub> afforded moderate adsorption energy, which was favorable of the reversible conversion and utilization of sulfur.

The activity of SACs strongly depends on the coordination of metal centers with the non-metallic atoms. Xie *et al.*<sup>[82]</sup> explored the relation between catalytic behaviors and electronic structures of different metal centers (Fe/Co/Ni) with similar physical and chemical properties in N-doped graphene. Combining the X-ray absorption spectroscopy, theoretical calculations, and electrochemical analysis, the coordination geometry and oxidation state of metal atoms interacting with sulfur were altered. As shown in Figure 4(d and e), it is revealed that enhanced kinetics process is closed in the distance near Fermi level. Moderate hybridization of the Fermi level with the metal 3d band was more favourable for the Li–S redox reaction. Han *et al.*<sup>[24]</sup> also developed a universal and controllable approach to synthesize a series of TM–N<sub>4</sub> SACs, with the metal center varying from Sc to Cu. It is still ambiguous to identify that which metal centers can better enhance the catalytic activity without accurate mechanism understanding. Generally, there are five types of  $d$  orbitals which can be marked as  $d_z^2$ ,  $d_{xy}$ ,  $d_{xz}$ ,  $d_{yz}$  and  $d_{x^2-y^2}$ . In consideration of the orbital symmetry, the  $d$ – $p$  hybridization pattern can be predicted in Figure 4(g), where the  $d_z^2$  orbital hybridizes with the  $p_z$  orbital of sulfur, leading to the formation of  $\sigma$  and  $\sigma^*$  bonds along with the strong energy splitting. They reported that the Ti single atom with only a few filled  $\pi^*$  states became the promising center with the most effective  $d$ – $p$  hybridization. Benefiting from the rational coordination, even under the high sulfur loadings of 4 and 8 mg cm<sup>-2</sup>, the SATi still endows the battery with more favorable capacity than other SACs (Figure 4h). In Li–S realm, the current investigation of metal centers in SACs mainly refers to one type rather than two or multi types, implying that there is enough space to allow the further coordination environment modulation. Despite of many foreseeable difficulties in the design approach and mechanism understanding, the metal center-determined activity of SACs would shed light on the construction of highly efficient Li–S batteries.

### 3.4. Integration with other active moieties

Apart from the high atom utilization efficiency, the atom loading also displays a critical impact on the electrochemical reaction and the final battery performance for the coordination-modulated SACs.<sup>[84,85]</sup> However, limited by the current synthesis routes and techniques, it's relatively difficult for the

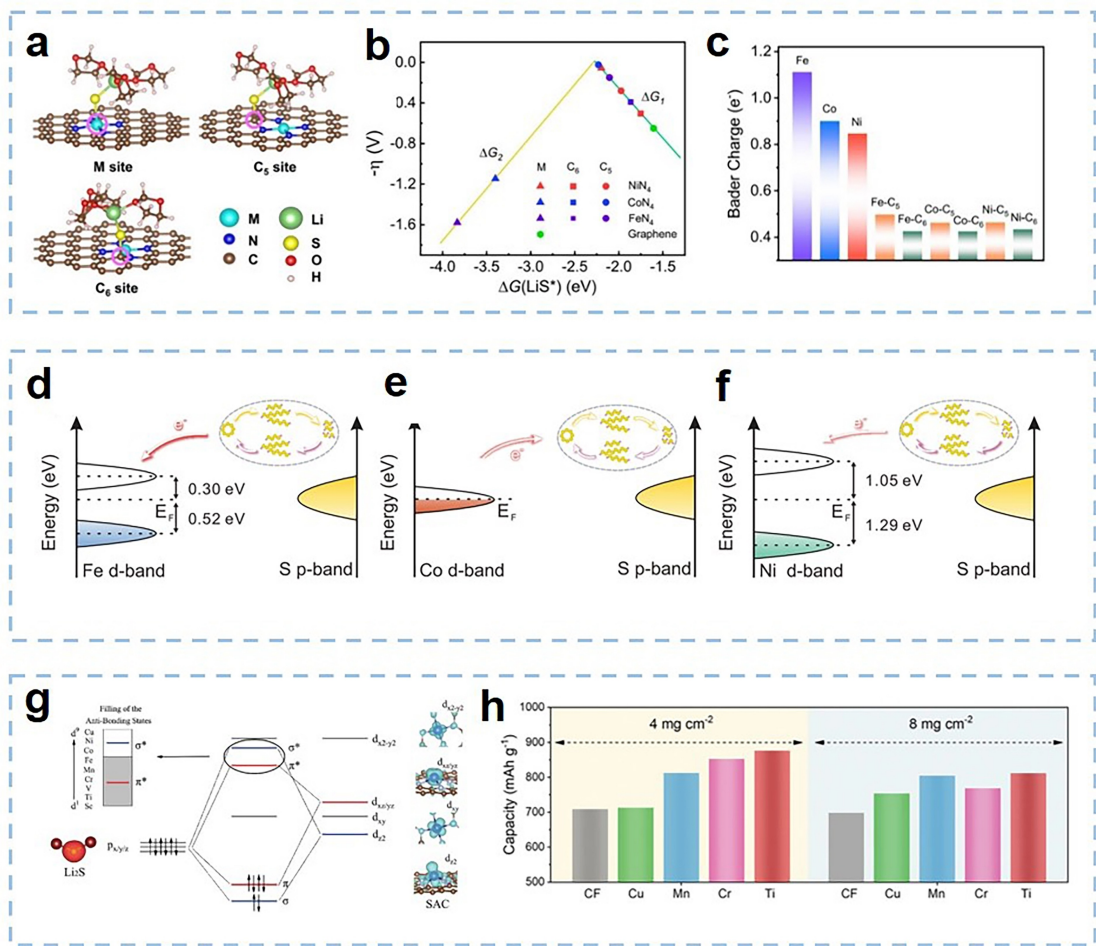


**Figure 4.** a) Optimized adsorption configurations of solvated  $\text{LiS}^*$  intermediate with the first explicit solvation shell (DOL molecule) on three representative sites, e.g., one metal site and two carbon sites in the five-membered ( $\text{C}_5$ ) and six-membered ring ( $\text{C}_6$ ). b) Volcano curve between the negative overpotential and adsorption free energy of  $\text{LiS}^*$  on the above active sites (triangles, squares, circles, and hexagon indicates the M,  $\text{C}_5$ ,  $\text{C}_6$  site of  $\text{MN}_4\text{C}_4$  and C site of pristine graphene, respectively). c) Bader charge analysis of M,  $\text{C}_5$ , and  $\text{C}_6$  site in the  $\text{MN}_4\text{C}_4$ -graphene. Reproduced with permission from Ref. [83]. Copyright (2022) Wiley-VCH. d-f) Schematic illustration of the local electronic structure of Fe/Co/Ni 3d-orbitals near the Fermi level and the S p-orbitals structure of sulfur species. Reproduced with permission from Ref. [82]. Copyright (2022) Wiley-VCH. g) d-p orbital hybridization scenario between SAC and  $\text{Li}_2\text{S}$ . Spatial charge density for SA-Ti and  $\text{Li}_2\text{S}$ , exhibiting the typical d-orbital and p-orbital distribution pattern. h) Capacities of different cathodes at 0.5 C with different sulfur loadings. Reproduced with permission from Ref. [24]. Copyright (2021) Wiley-VCH.

SACs to possess sufficient atom loading. Recent years have witnessed fruitful advancements in introducing other active sites/moieties such as nanoparticles and vacancies<sup>[86–88]</sup> into the SAC supports to construct a novel electrocatalyst system. These well-designed catalyst systems integrate the local isolated metal atoms and the foreign active centers to pledge the reaction efficiency of the whole cathode. Such a strategy can fill the research gap of SACs to a certain extent and offer new insights into the design of effective catalysts for Li–S chemistry.

Zhao *et al.*<sup>[89]</sup> reported a unique catalyst system composing of Co–N–C SAC and uniformly embedded ZnS nanoparticles to form double-end binding sites (DEB) inside a highly oriented macroporous host (Figure 5a). Polar metal composites modulated coordination environment around Co atoms, which successfully immobilized LiPSs and promoted sulfur redox reaction kinetics. With the assistance of ZnS particles, the cathode presents remarkable capacity values among all samples (Figure 5b). More importantly, the thus-designed

structure holds great promise for practical applications. The pouch cell was assembled and tested at different current densities. Figure 5c shows that an as-prepared 100-mg-level pouch cell can achieve over  $800 \text{ mAh g}^{-1}$  specific capacity for 60 cycles with a current density of  $200 \text{ mAh g}^{-1}$ . Ma *et al.*<sup>[90]</sup> proposed an effective “outside” design strategy to prevent the LiPSs from escape by integrating Fe SA and  $\text{Fe}_2\text{N}$  compound into a SA–Fe/ $\text{Fe}_2\text{N}$ @NG system. For SA–Fe@NG, the limited active site number and weak interaction are adverse to trapping LiPSs and providing effective catalytic ability. Nevertheless, the efficient and sufficient active sites could be created after introducing the  $\text{Fe}_2\text{N}$ . The SA–Fe/ $\text{Fe}_2\text{N}$ @NG separator utilizes the synergistic sites to promote the reduction and oxidation of sulfur species (Figure 5d). In terms of precipitation and decomposition of  $\text{Li}_2\text{S}$ , the redox peaks of SA–Fe/ $\text{Fe}_2\text{N}$ @NG-based battery exhibit earlier and higher current response than SA–Fe@NG and NG-based batteries (Figure 5e and f), demonstrating the facilitated bidirectional catalytic

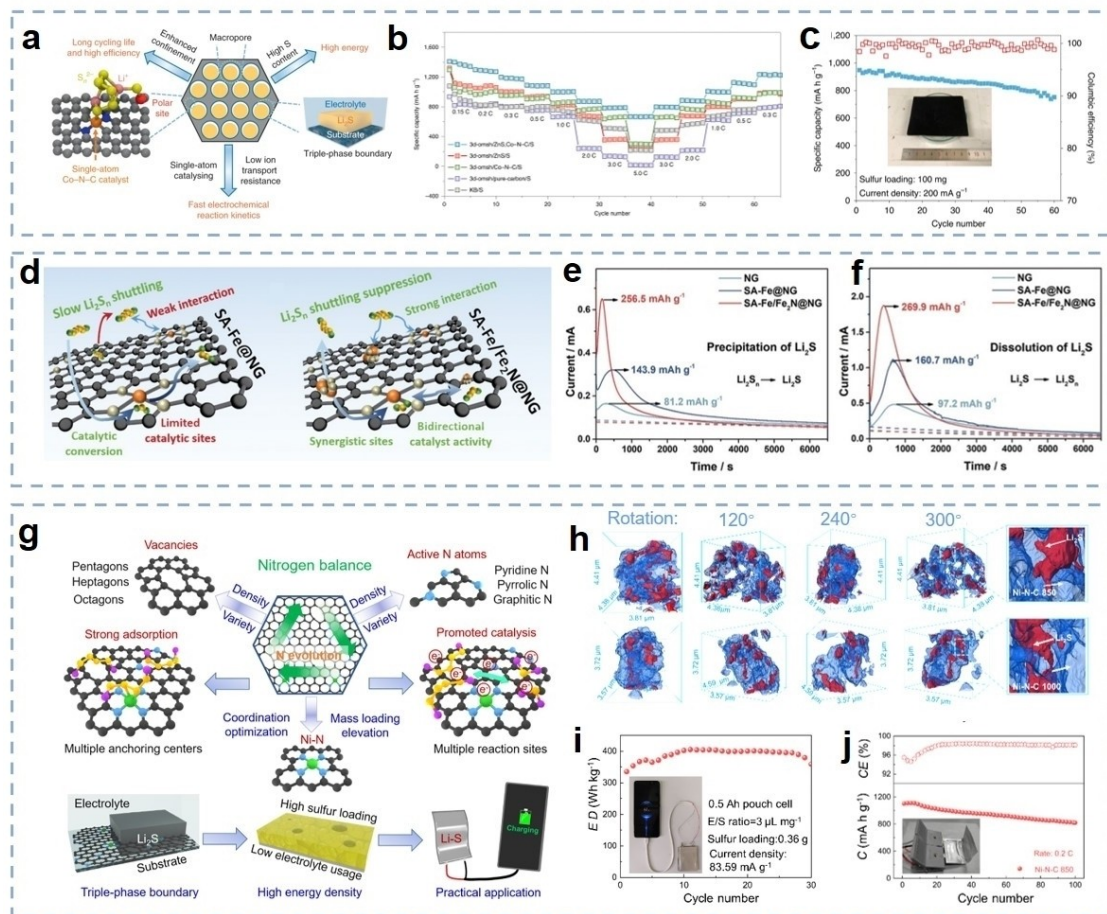


**Figure 5.** a) Design strategy of macro-porous host with DEB sites. b) Rate capability of various sulfur cathodes. c) Capacity retention of 100-mg-sulfur pouch cell using 3d-omsh/ZnS, Co-N/C/S cathode. Inset: digital photo of the as-prepared 6 cm × 8 cm cathode. Reproduced with permission from Ref. [89]. Copyright (2020) Nature. d) Schematically illustrating the mechanism of polysulfide adsorption/conversion on SA-Fe@NG and SA-Fe/Fe<sub>2</sub>N@NG. e, f) Potentiostatic discharge and charge profiles at 2.05 and 2.40 V for the nucleation and decomposition of Li<sub>2</sub>S on the surfaces of NG, SA-Fe, and SA-Fe/Fe<sub>2</sub>N@NG. Reproduced with permission from Ref. [90]. Copyright (2021) Wiley-VCH. g) Schematic illustration of all-in-one “nitrogen balance” for maximizing the electrocatalytic activity of Ni–N–C system. h) Synchrotron X-ray 3D nano-CT images with respect to Li<sub>2</sub>S deposits on Ni–N–C substrates under various rotation angles. i) Cycling performance of S/Ni–N–C 850 with the folding angle of 90°. j) Capacity retention of (0.36 g-sulfur) pouch cell with the Ni–N–C 850 as the electrocatalyst, with the inset showing the diagram of charging mobile phone by two pouch cells connected in series. Reproduced with permission from Ref. [91]. Copyright 2022, Wiley-VCH.

activity and adsorption to LiPSs. The above-mentioned catalyst systems imply the synergy mechanism of single atom and nanoclusters for Li–S redox reactions.

Our recent work reported the active V–N–C system integrating with twinborn isolated V single atoms and ultra-small-sized VN nanoparticles for manipulating Li–S chemistry.<sup>[86]</sup> Particularly, we deciphered the synergy and division mechanism of the dual V-based centers. Such system can usually make full use of the property merits of the components to show the superior catalytic activity. The combined merits involved highly utilized V single atoms, modulated V–N–C coordination as well as site-rich VN. The division mechanism could be disclosed by calculating the LiPS adsorption energies, Li<sub>2</sub>S decomposition energy barriers and identifying the rate-determining steps accordingly. The soft-packaged pouch cells usually call for more powerful catalysts to approach the practical application. In light of this, we also proposed a versatile “N balance” strategy to design an active Ni–N–C

system for Li–S pouch cells.<sup>[91]</sup> The “N balance” strategy pertains to the temperature-triggered N operation including essential subtraction, reservation and coordination in Ni–N–C system for managing the Ni–N coordination form, Ni sing atom loading, active N level, vacancy density simultaneously and the electron conductivity (Figure 5g). Multiple centers assisted the coordinated Ni single atoms to maximize the electrocatalysis activity of Ni–N–C system. The electrokinetic control of Li<sub>2</sub>S precipitation reaction can be fulfilled by tuning the surface area, adsorption strength, conductivity, etc., implying the typical Li<sub>2</sub>S nucleation mechanism for Li–S batteries. The Li<sub>2</sub>S nucleation and decomposition mass in this investigation also confirmed the corresponding elevated reaction kinetics resulting from the Ni–N–C system. After the Li<sub>2</sub>S nucleation test, the samples were gathered from the disassembled cells for further characterizations. The synchrotron three-dimensional nano-computed tomography (X-ray 3D nano-CT) results demonstrate the higher mass proportion, smaller size and more homogeneous spatial

distribution of  $\text{Li}_2\text{S}$  product in the optimized Ni–N–C system in comparison with the control (Figure 5h). As a result, the pouch cell harvested a remarkable energy density of 405.1  $\text{Wh kg}^{-1}$  (Figure 5i–j). This integrating strategy holds a new insight to the SAC design principle. It is worthy of extending this proposal to realize the rational combination of SACs with other active centers targeted high-performance Li–S batteries.

### 3.5. Supportive substrates

The supports can not only be used to load and anchor metal single atoms but also tune the coordination environments of SACs. Such a support effect has received ever-increasing attention by far in Li–S realm. Selecting suitable supporting candidates or modulating geometric configurations might change the coordination environment around the metal centers.<sup>[92,93]</sup> A morphological modification in graphene was proposed by Kim *et al.*<sup>[94]</sup> They accurately introduced defects into the two-dimensional (2D) graphene, and subsequently bond lengths and angles were changed because of the additional planar stress, leading to formation of specific

wrinkled structure. There is an obvious fluctuation in the FeNC/wG in contrast to the FeNC/G (Figure 6a), thus leading to exposing more active sites on nonplanar surface. XANES spectra were used to identify the chemical state of Fe. As exhibited in Figure 6b, the distinct pre-edge peaks in FeNC/wG and FeNC/G suggest the lattice distortion and structure improvement, which is conducted to boosting the sulfur redox reaction kinetics. Owing to the modulated coordination of Fe–N<sub>4</sub>–C by the support of wG, the battery exhibited remarkable performance under high rates. In another study, a high Fe atom loading up to 8.5 wt.% was achieved by using 2D C<sub>3</sub>N<sub>4</sub> substrate.<sup>[85]</sup> Inspired by these results, one of our recent studies designed an unsaturated Fe–N<sub>2</sub> system embedded in a 3D hierarchical C<sub>3</sub>N<sub>4</sub> architecture (3DFeSA-CN) by virtue of bio-templated method.<sup>[95]</sup> The 3D carbon matrix had a larger specific surface area, which allowed the large coordination concentration. As seen from Figure 6(e), the obvious right shift of cathodic peaks and left shift of anodic peak in CV curves of S@3DFeSA-CN cathode compared with other samples demonstrate that such coordination modulation endows the batteries with faster electron/ion transfer, and thus elevated dual-directional sulfur redox kinetics. In addition, the larger current

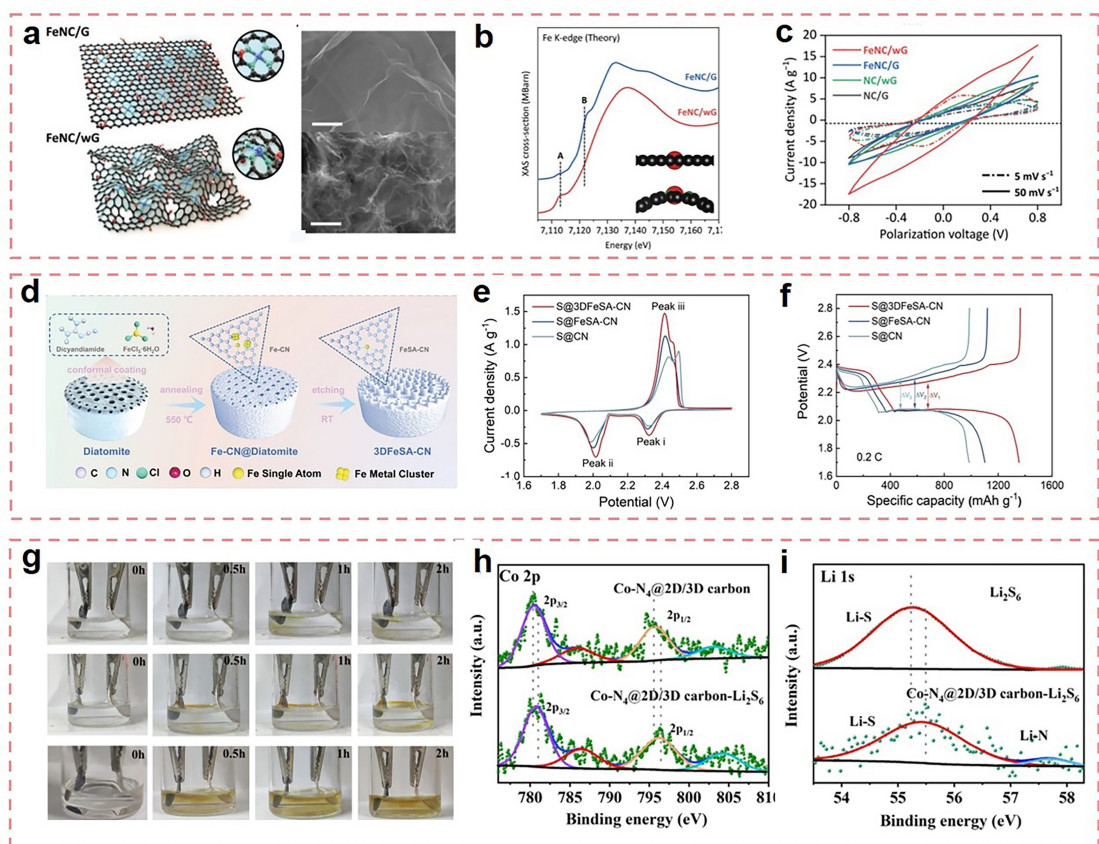


**Figure 6.** a) Illustration of Fe–N<sub>x</sub> sites on planar graphene (FeNC/G, top) and wG (FeNC/wG, bottom) and scanning electron microscope (SEM) images of FeNC/G (top) and FeNC/wG (bottom) (scale bar, 0.5  $\mu\text{m}$ ). b) Calculated XANES spectra based on the DFT-based models. c) CV curves of symmetric cells with 0.5 M  $\text{Li}_2\text{S}_6$  solutions at scan rates of 5 and 50  $\text{mV s}^{-1}$ . a–c) Reproduced with permission from Ref. [94]. Copyright (2022) Wiley-VCH. d) Synthetic process of 3DFeSA-CN. e) Typical CV curves of S@3DFeSA-CN, S@FeSA-CN, and S@CN electrodes at 0.05  $\text{mV s}^{-1}$ . f) GCD profiles at 0.2 C. Reproduced with permission from Ref. [95]. Copyright (2022) Wiley-VCH. g) *In situ* beaker cell observation during discharge from 2.8 to 1.7 V at 0.1 C for S@Co–N<sub>4</sub>@2D/3D carbon, S@2D carbon, and S@Co–N<sub>4</sub>@carbon. h) The Co 2p XPS of spectra of Co–N<sub>4</sub>@2D/3D before and after adsorbing  $\text{Li}_2\text{S}_6$ . i) The Li 1s XPS spectra of  $\text{Li}_2\text{S}_6$  before and after being adsorbed with Co–N<sub>4</sub>@2D/3D carbon. Reproduced with permission from Ref. [96]. Copyright (2021) Springer Nature.

response and smaller voltage polarization also confirm the optimized sulfur reaction process (Figure 6f). It can be concluded that morphology engineering on supports can lead to the significant influence on LiPS conversion.

Similarly, throughout implanting Co–N<sub>4</sub> on porous 3D carbon architecture with the aid of a SiO<sub>2</sub>-mediated zeolitic imidazolate framework-L (ZIF-L) strategy, Wang *et al.*<sup>[96]</sup> reported Co–N<sub>4</sub> coordinated SAC by the support morphology regulation. An *in situ* beaker cell observation experiment was conducted to investigate the LiPS diffusion in the electrolyte. As shown in Figure 6(g), the change of color in electrolyte is difficult to be observed in S@Co–N<sub>4</sub>@2D/3D, substantiating the stronger adsorption with LiPSs, which matches well with the right shift of peaks in XPS characterizations (Figure 6h and i). As a control, the colors of electrolyte in S@2D carbon and S@Co–N<sub>4</sub>@2D carbon clearly turn to yellow, indicating that LiPS intermediates are severely dissolved into electrolyte. It's worth-noting that the use of template or confine route can serve as an effective strategy to tune the coordination concentration. In addition, defect engineering is of importance to the coordination manipulation of SACs. The designing approaches including H<sub>2</sub>O<sub>2</sub> etching<sup>[97]</sup> and plasma irradiation<sup>[98]</sup> could be used. Besides the carbon supports, other supports such as metal compounds may also give rise to the modulated coordination structures. The support effect presents strong correlation with the coordination environment and concentration, which can contribute to the efficient coordination engineering.

## 4. Conclusions and Outlooks

Li–S batteries have made a huge leap forward in the past decades. From bulk to nano size, the metal-based catalysts have been designed to boost the Li–S battery performance. However, the obstacles of shuttle effect and sluggish kinetics are still formidable to be dealt with owing to the existing gap between theoretical and practical research of Li–S batteries. Tremendous efforts have been devoted to addressing these problems but rarely fruitful achievements are produced. Fortunately, SACs as a promising candidate bring more possibilities for Li–S batteries. In this review, we systematically include the state-of-the-art progresses on the coordination modulation of SACs for Li–S batteries. First, we can find that the coordination environment modulation plays a vital role in the activity design of SACs, not only leading to the acceleration of bidirectional LiPS conversion kinetics but also strengthening the LiPS adsorption ability. By modulating coordinated atom number, atom type, metal atom centers, supports and integration with other introduced moieties, the activity of SACs can be further elevated. Herein, we proficiently make use of theoretical analysis and experimental advances to guide the effective activity elevation of SACs, gain further understanding of the related mechanism, and promote the commercial viability of Li–S batteries. The representative advances of SAC-enabled battery performance are listed in Table 1.

Nevertheless, many spaces are still waiting for the future explorations. These involve, but not limited to, the following aspects (Figure 7):

**Table 1.** The electrochemical performances of Li–S batteries based on SAC mediators.

Mediator	Modulation strategy	Sulfur loading [mg cm <sup>-2</sup> ]	Capacity at low rate [mAh g <sup>-1</sup> ]	Capacity at high rate [mAh g <sup>-1</sup> ]	Cycles (rate)/Decay rate [%]	Ref.
FeSA–PCNF	Coordination number	17	1183 (0.2 C)	791 (5 C)	500 (2 C)/0.048	[70]
Mo–N–CNF	Coordination number	5.1	1248 (0.2 C)	715 (5 C)	400(1 C)/0.062	[66]
Sn <sub>SA</sub> –NC	Coordination number	5	1233 (0.2 C)	687@2 C 603@3 C	300 (0.5 C)/0.110 300 (1 C)/0.031	[68]
Ni@NG	Coordination number	6	1598 (0.1 C)	612 (10 C)	500 (10 C)/0.06	[42]
SC–Co	Coordination number	3.6	1130 (0.5 C)	810 (3 C)	300 (0.5 C)/0.086	[63]
FeN <sub>2</sub> –NC	Coordination number	5	1397 (0.2 C)	760 (5 C)	500 (1 C)/0.055	[71]
Fe–N <sub>2</sub> /CN	Coordination number	5.6	1301 (0.2 C)	607 (5 C)	2000 (2 C)/0.011	[65]
Mo–N <sub>2</sub> /C	Coordination number	8	1360.2 (0.1 C)	743.9 (5 C)	550 (2 C)/0.018	[64]
Fe–N <sub>5</sub> –C	Coordination number	8.2	1170 (0.2 C)	723 (3 C)	500 (1 C)/0.054	[73]
Ni–N <sub>5</sub> /HNPC	Coordination number	5.1	1188 (0.2 C)	684 (4 C)	500 (0.5 C)/0.053	[74]
Co/SA–Zn@NC/CNTs	Integration	5.1	932 (1 C)	–	800 (1 C)/0.033	[89]
V–N–C	Integration	8.1	1132.5 (0.2 C)	609.3 (2 C)	1000 (2 C)/0.052	[86]
SA–Fe/Fe <sub>2</sub> N@NG	Integration	5	936.4 (1 C)	736.5 (4 C)	500 (1 C)/0.0318	[90]
W/NG	Non-metallic atom type	8.3	1389 (0.2 C)	678 (10 C)	500 (1 C)/0.07 1000 (2 C)/0.045	[78]
FeSA–PN@PNC	Non-metallic atom type	6.4	1114 (0.2 C)	659 (2 C)	800 (1 C)/0.04	[79]
Mn/C–(N,O)	Non-metallic atom type	4	1330 (0.2 C)	900 (1 C)	1000 (1 C)/0.05	[77]
Fe–N <sub>5</sub> C <sub>2</sub> –C	Non-metallic atom type	6.6	931 (2 C)	846 (4 C)	1000 (2 C)/0.053	[80]
SATi@CF	Metal center	8	1151 (0.2 C)	634 (3 C)	300 (0.5 C)/0.027	[24]
NiSA PCNF	Metal center	10.2	1505.5 (0.2 C)	940.4 (3 C)	500 (1 C)/0.09	[83]
SA–Cu@NCNF	Metal center	10	499 after 200 cycles at 1 C	400 after 500 cycles at 5 C	500 (5 C)/0.038	[99]
3DFeSA–CN	Support effect	5.75	1114.4 (0.5 C)	–	2000 (1 C)/0.031	[95]
SA–Zn–MXene	Support effect	5.3	1136 (0.2 C)	517 (6 C)	400 (4 C)/0.03	[92]
Co–PCNF	Support effect	6.9	1373.5 (0.2 C)	914.3 (2 C)	800 (1 C)/0.05	[20]
CoN <sub>4</sub> @2D/3D carbon	Support effect	4.6	805 (2 C)	695 (5 C)	500 (1 C)/0.053	[96]
FeNC/wG	Support effect	5.39	–	915.9 (5 C)	300 (4 C)/0.0014	[94]
Pt SAs/In <sub>2</sub> S <sub>3</sub> /Ti <sub>3</sub> C <sub>2</sub>	Support effect	6.4	1068.4 (0.5 C) 949.7 (1 C)	866.1 (2 C)	1000 (0.2 C)/0.031	[93]

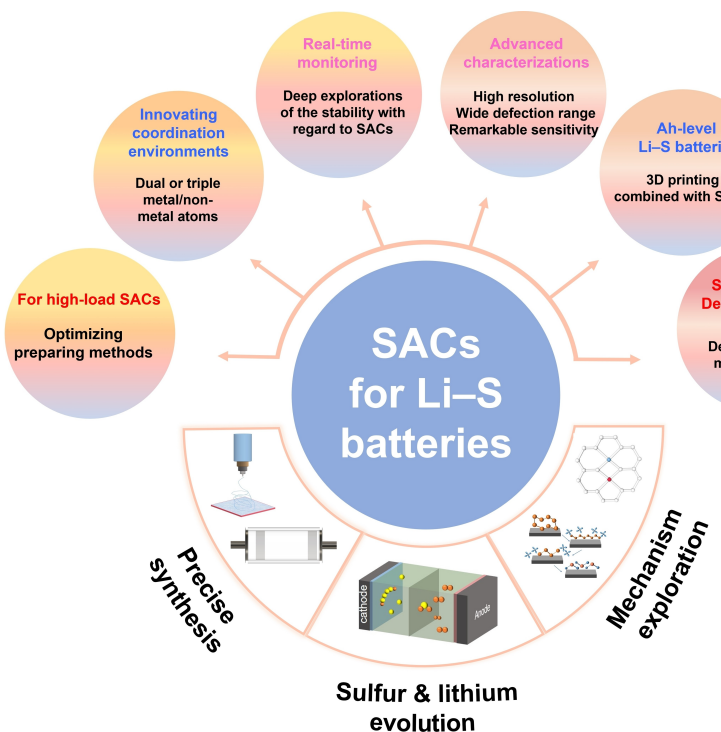


Figure 7. Future directions for SACs in Li–S batteries.

- i) **Optimizing synthetic strategies for high-loading SACs.** The loading of metal centers in SACs strongly correlates with the sulfur evolution tuning in a LiPS-flooded battery system. The recently reported metal center loading in SACs is relatively low (usually less than 5 wt%). To increase the metal loading, surface area augmentation and defect density tuning with regards to the support might act as feasible strategies.
- ii) **Innovating the coordination environments for highly active SACs.** The current coordination investigations of SACs mainly refer to the coordinated atom number, metal/non-metal atom type, synergy with other foreign clusters, accompanied by the support design in Li–S realm. The coordination diversity could be further enhanced. For instance, the cooperation of dual or triple metal/non-metal atoms could enrich the coordination environments. In this sense, machine learning holds the promise for screening the coordination environments, which helps to pinpoint the active SACs with preferred coordination configurations according to the database comprising LiPS adsorption energies, rate-limiting steps and  $\text{Li}_2\text{S}$  decomposition energy barriers.
- iii) **Elevating the stability of SACs when experiencing sulfur redox.** The activity of the SACs can be well enhanced by virtue of the coordination modulation. However, the stability of SACs throughout the whole discharge/charge procedure has been rarely probed thus far. Considering this, systematic explorations of the stability should be performed. Of note, the real-time monitoring of the coordination form is essential and necessary.
- iv) **Exploiting advanced characterization toolbox for the catalyst monitoring.** With the consideration of metastable states of sulfur species in a practically-operated Li–S battery, the currently employed spectroscopic toolsets are insufficient to record this information in real time, which results in a multitude of challenges to evaluating the coordination stability and probe the working mechanism of SACs. Therefore, characterization facilities with high resolution, wide deflection range and remarkable sensitivity are highly demanding.
- v) **Deciphering the roles of SACs played in cathodes and anodes.** To date, extensive efforts have been paid to the issues of shuttle effect and sluggish redox kinetics at the sulfur cathode. Nevertheless, the simultaneous investigation of sulfur cathode and lithium anode are in its infancy. The combination of complex sulfur conversion and intricate lithium evolution behaviors poses a great threat to the underlying understanding of the roles of SACs. Therefore, endeavors from both theoretical simulations and experimental characterizations would be further made.
- vi) **Extending the uses of SACs in Ah-level Li–S batteries.** Versatile 3D printing technique is conducive to the construction of self-standing sulfur cathodes with ample pore structures. Hence, considering the intractable issues in high-loading sulfur cathode for soft-packaged pouch cells, combining the active SACs with 3D printing technique can make full use of the own merits to facilitate the fabrication of Ah-level Li–S batteries with satisfying performance. At present, such a strategy has been rarely exploited, leaving a research gap in this realm.

## Acknowledgements

This work was supported by the National Natural Science Foundation of China (22179089 and 52172239), Science Fund for Distinguished Young Scholars of Jiangsu Province (BK20211503), Suzhou Science and Technology Project-Promotive Application Research Program (SYG202038), Project of State Key Laboratory of Environment-Friendly Energy Materials (SWUST, 22fksy23 and 18ZD320304) and Frontier Project of Chengdu Tianfu New Area Institute (SWUST, 2022ZY017).

## Conflict of Interest

The authors declare no conflict of interest.

**Keywords:** activity design • coordination modulation • lithium-sulfur battery • single atom catalysts

- [1] Z. Shi, Z. Sun, J. Cai, X. Yang, C. Wei, M. Wang, Y. Ding, J. Sun, *Adv. Mater.* **2021**, *33*, 2103050.
- [2] J. Cai, Z. Sun, W. Cai, N. Wei, Y. Fan, Z. Liu, Q. Zhang, J. Sun, *Adv. Funct. Mater.* **2021**, *31*, 2100586.
- [3] C. Lu, Z. Gao, B. Liu, Z. Shi, Y. Yi, W. Zhao, W. Guo, Z. Liu, J. Sun, *Adv. Funct. Mater.* **2021**, *31*, 2101233.
- [4] M. Wang, Z. Sun, H. Ci, Z. Shi, L. Shen, C. Wei, Y. Ding, X. Yang, J. Sun, *Angew. Chem. Int. Ed.* **2021**, *60*, 24558–24565; *Angew. Chem.* **2021**, *133*, 24763–24770.
- [5] B. Guan, X. Sun, Y. Zhang, X. Wu, Y. Qiu, M. Wang, L. Fan, N. Zhang, *Chin. Chem. Lett.* **2021**, *32*, 2249–2253.
- [6] M. Ji, J. Ni, X. Liang, Q. Cheng, G. Gao, G. Wu, Q. Xiao, *Adv. Funct. Mater.* **2022**, *22065*.
- [7] J. L. Cheong, C. Hu, W. Liu, M.-F. Ng, M. B. Sullivan, J. Y. Ying, *Nano Energy* **2022**, *102*, 107659.
- [8] J. Qian, Y. Xing, Y. Yang, Y. Li, K. Yu, W. Li, T. Zhao, Y. Ye, L. Li, F. Wu, R. Chen, *Adv. Mater.* **2021**, *33*, 2100810.
- [9] J. Yu, J. Xiao, A. Li, Z. Yang, L. Zeng, Q. Zhang, Y. Zhu, L. Guo, *Angew. Chem. Int. Ed.* **2020**, *59*, 13071–13078; *Angew. Chem.* **2020**, *132*, 13171–13178.
- [10] Q. Wang, H. Zhao, B. Li, C. Yang, M. Li, Y. Li, P. Han, M. Wu, T. Li, R. Liu, *Chin. Chem. Lett.* **2021**, *32*, 1157–1160.
- [11] C. Yang, N. Gong, T. Chen, Y. Li, W. Peng, F. Zhang, X. Fan, *Green Energy & Environ.* **2022**, *7*, 1340–1348.
- [12] Z. Shi, Y. Ding, Q. Zhang, J. Sun, *Adv. Energy Mater.* **2022**, *12*, 2201056.
- [13] H. Fei, J. Dong, D. Chen, T. Hu, X. Duan, I. Shakir, Y. Huang, X. Duan, *Chem. Soc. Rev.* **2019**, *48*, 5207–5241.
- [14] J. Wu, J. Chen, Y. Huang, K. Feng, J. Deng, W. Huang, Y. Wu, J. Zhong, Y. Li, *Sci. Bull.* **2019**, *64*, 1875–1880.
- [15] H. Zhao, B. Tian, C. Su, Y. Li, *ACS Appl. Mater. Interfaces* **2021**, *13*, 7171–7177.
- [16] X. Zhang, Y. Zhang, X. Wei, C. Wei, Y. Song, *Nanoscale Adv.* **2021**, *3*, 5777–5784.
- [17] B. Qiao, A. Wang, X. Yang, L. F. Allard, Z. Jiang, Y. Cui, J. Liu, J. Li, T. Zhang, *Nat. Chem.* **2011**, *3*, 634–641.
- [18] M. Jiang, F. Wang, F. Yang, H. He, J. Yang, W. Zhang, J. Luo, J. Zhang, C. Fu, *Nano Energy* **2022**, *93*, 106793.
- [19] C. L. Song, Z. H. Li, L. Y. Ma, M. Z. Li, S. Huang, X. J. Hong, Y. P. Cai, Y. Q. Lan, *ACS Nano* **2021**, *15*, 13436–13443.
- [20] T. Huang, Y. Sun, J. Wu, J. Jin, C. Wei, Z. Shi, M. Wang, J. Cai, X. T. An, P. Wang, C. Su, Y. Y. Li, J. Sun, *ACS Nano* **2021**, *15*, 14105–14115.
- [21] Y. Wang, Y. Wei, B. Wang, P. Jing, Y. Zhang, Y. Zhang, Q. Wang, H. Wu, *Carbon* **2021**, *177*, 60–70.
- [22] D.-R. Deng, C. Li, J.-C. Weng, X.-H. Fan, Z.-J. Chen, G. Yang, Y. Li, Q.-H. Wu, M.-S. Zheng, Q.-F. Dong, *ACS Appl. Mater. Interfaces* **2022**, *14*, 45414–45422.
- [23] Y. Li, S. Lin, D. Wang, T. Gao, J. Song, P. Zhou, Z. Xu, Z. Yang, N. Xiao, S. Guo, *Adv. Mater.* **2020**, *32*, 1906722.
- [24] Z. Han, S. Zhao, J. Xiao, X. Zhong, J. Sheng, W. Lv, Q. Zhang, G. Zhou, H. M. Cheng, *Adv. Mater.* **2021**, *33*, 2105947.
- [25] G. Zhou, S. Zhao, T. Wang, S. Z. Yang, B. Johannessen, H. Chen, C. Liu, Y. Ye, Y. Wu, Y. Peng, C. Liu, S. P. Jiang, Q. Zhang, Y. Cui, *Nano Lett.* **2020**, *20*, 1252–1261.
- [26] E. I. Andritsos, C. Lekakou, Q. Cai, *J. Phys. Chem. C* **2021**, *125*, 18108–18118.
- [27] Z. Liang, D. Yang, P. Tang, C. Zhang, J. Jacas Biendicho, Y. Zhang, J. Llorca, X. Wang, J. Li, M. Heggen, J. David, R. E. Dunin-Borkowski, Y. Zhou, J. R. Morante, A. Cabot, J. Arbiol, *Adv. Energy Mater.* **2020**, *11*, 2003507.
- [28] Y. Wang, C. Shi, J. Sha, L. Ma, E. Liu, N. Zhao, *ACS Appl. Mater. Interfaces* **2022**, *14*, 25337–25347.
- [29] A. Shan, X. Teng, Y. Zhang, P. Zhang, Y. Xu, C. Liu, H. Li, H. Ye, R. Wang, *Nano Energy* **2022**, *94*, 106913.
- [30] P. Su, W. Pei, X. Wang, Y. Ma, Q. Jiang, J. Liang, S. Zhou, J. Zhao, J. Liu, G. Q. Lu, *Angew. Chem. Int. Ed.* **2021**, *60*, 16044–16050; *Angew. Chem.* **2021**, *133*, 16180–16186.
- [31] Y. Sun, Z. Xue, Q. Liu, Y. Jia, Y. Li, K. Liu, Y. Lin, M. Liu, G. Li, C.-Y. Su, *Nat. Commun.* **2021**, *12*, 1369.
- [32] Y. He, X. Yang, Y. Li, L. Liu, S. Guo, C. Shu, F. Liu, Y. Liu, Q. Tan, G. Wu, *ACS Catal.* **2022**, *12*, 1216–1227.
- [33] M. Ha, D. Y. Kim, M. Umer, V. Gladkikh, C. W. Myung, K. S. Kim, *Energy Environ. Sci.* **2021**, *14*, 3455–3468.
- [34] S.-N. Zhao, J.-K. Li, R. Wang, J. Cai, S.-Q. Zang, *Adv. Mater.* **2022**, *34*, 2107291.
- [35] H. Huang, D. Yu, F. Hu, S.-C. Huang, J. Song, H.-Y. Chen, L. L. Li, S. Peng, *Angew. Chem. Int. Ed.* **2022**, *61*, 2116068.
- [36] Z. Zhu, H. Yin, Y. Wang, C.-H. Chuang, L. Xing, M. Dong, Y.-R. Lu, G. Casillas-Garcia, Y. Zheng, S. Chen, Y. Dou, P. Liu, Q. Cheng, H. Zhao, *Adv. Mater.* **2020**, *32*, 2004670.
- [37] Y. Guo, S. Yao, Y. Xue, X. Hu, H. Cui, Z. Zhou, *Appl. Catal. B* **2022**, *304*, 120997.
- [38] X. Sun, Y. Tuo, C. Ye, C. Chen, Q. Lu, G. Li, P. Jiang, S. Chen, P. Zhu, M. Ma, J. Zhang, J. H. Bitter, D. Wang, Y. Li, *Angew. Chem. Int. Ed.* **2021**, *60*, 23614–23618; *Angew. Chem.* **2021**, *133*, 23806–23810.
- [39] Y. Gu, B. Xi, W. Tian, H. Zhang, Q. Fu, S. Xiong, *Adv. Mater.* **2021**, *33*, 2100429.
- [40] Y. Li, J. Li, J. Huang, J. Chen, Y. Kong, B. Yang, Z. Li, L. Lei, G. Chai, Z. Wen, L. Dai, Y. Hou, *Angew. Chem. Int. Ed.* **2021**, *60*, 9078–9085; *Angew. Chem.* **2021**, *133*, 9160–9167.
- [41] F. Lü, S. Zhao, R. Guo, J. He, X. Peng, H. Bao, J. Fu, L. Han, G. Qi, J. Luo, X. Tang, X. Liu, *Nano Energy* **2019**, *61*, 420–427.
- [42] L. Zhang, D. Liu, Z. Muhammad, F. Wan, W. Xie, Y. Wang, L. Song, Z. Niu, J. Chen, *Adv. Mater.* **2019**, *31*, 1903955.
- [43] Z. Du, X. Chen, W. Hu, C. Chuang, S. Xie, A. Hu, W. Yan, X. Kong, X. Wu, H. Ji, L. J. Wan, *J. Am. Chem. Soc.* **2019**, *141*, 3977–3985.
- [44] Y. Miao, Y. Zheng, F. Tao, Z. Chen, Y. Xiong, F. Ren, Y. Liu, *Chin. Chem. Lett.* **2023**, *34*, 107121.
- [45] Y. Song, L. Zou, C. Wei, Y. Zhou, Y. Hu, *Carbon Energy* **2022**, DOI: 10.1002/cey2.286.
- [46] Z. Liang, J. Shen, X. Xu, F. Li, J. Liu, B. Yuan, Y. Yu, M. Zhu, *Adv. Mater.* **2022**, *34*, 2200102.
- [47] F. Wang, J. Li, J. Zhao, Y. Yang, C. Su, Y. L. Zhong, Q. H. Yang, J. Lu, *ACS Materials Lett.* **2020**, *2*, 1450–1463.
- [48] M. Gao, W. Zhou, Y. Mo, T. Sheng, Y. Deng, L. Chen, K. Wang, Y. Tan, H. Zhou, *Adv. Powder Mater.* **2022**, *1*, 100006.
- [49] D. H. S. Tan, Y.-T. Chen, H. Yang, W. Bao, B. Sreenarayanan, J.-M. Doux, W. Li, B. Lu, S.-Y. Ham, B. Sayahpour, J. Scharf, E. A. Wu, G. Deysher, H. E. Han, H. J. Hah, H. Jeong, J. B. Lee, Z. Chen, Y. S. Meng, *Science* **2021**, *373*, 1494–1499.
- [50] S. Zhao, Y. Kang, M. Liu, B. Wen, Q. Fang, Y. Tang, S. He, X. Ma, M. Liu, Y. Yan, *J. Mater. Chem. A* **2021**, *9*, 18927–18946.
- [51] Z. Shi, M. Li, J. Sun, Z. Chen, *Adv. Energy Mater.* **2021**, *11*, 2100332.
- [52] L. Peng, Z. Wei, C. Wan, J. Li, Z. Chen, D. Zhu, D. Baumann, H. Liu, C. S. Allen, X. Xu, A. I. Kirkland, I. Shakir, Z. Almutairi, S. Tolbert, B. Dunn, Y. Huang, P. Sautet, X. Duan, *Nat. Catal.* **2020**, *3*, 762–770.
- [53] J. Tan, M. Ye, J. Shen, *Mater. Horiz.* **2022**, *9*, 2325–2334.
- [54] H. Shi, X. Ren, J. Lu, C. Dong, J. Liu, Q. Yang, J. Chen, Z. S. Wu, *Adv. Energy Mater.* **2020**, *10*, 2002271.
- [55] F. Liu, G. Sun, H. B. Wu, G. Chen, D. Xu, R. Mo, L. Shen, X. Li, S. Ma, R. Tao, X. Li, X. Tan, B. Xu, G. Wang, B. S. Dunn, P. Sautet, Y. Lu, *Nat. Commun.* **2020**, *11*, 5215.
- [56] X. Sun, D. Tian, X. Song, B. Jiang, C. Zhao, Y. Zhang, L. Yang, L. Fan, X. Yin, N. Zhang, *Nano Energy* **2022**, *95*, 106979.

- [57] M. Wang, L. Fan, X. Sun, B. Guan, B. Jiang, X. Wu, D. Tian, K. Sun, Y. Qiu, X. Yin, Y. Zhang, N. Zhang, *ACS Energy Lett.* **2020**, *5*, 3041–3050.
- [58] X. Fan, S. Chen, W. Gong, X. Meng, Y. Jia, Y. Wang, S. Hong, L. Zheng, L. Zheng, C. W. Bielawski, J. Geng, *Energy Storage Mater.* **2021**, *41*, 14–23.
- [59] Z. Zeng, W. Nong, Y. Li, C. Wang, *Adv. Sci.* **2021**, *8*, 2102809.
- [60] H. Sun, Y. Ma, Q. Zhang, C. Su, *Trans. Tianjin Univ.* **2021**, *27*, 313–330.
- [61] W. Zheng, R. Zhu, H. Wu, T. Ma, H. Zhou, M. Zhou, C. He, X. Liu, S. Li, C. Cheng, *Angew. Chem. Int. Ed.* **2022**, *61*, 202208667.
- [62] X. Wu, H. Zhang, S. Zuo, J. Dong, Y. Li, J. Zhang, Y. Han, *Nano-Micro Lett.* **2021**, *13*, 136.
- [63] J. Xie, B. Q. Li, H. J. Peng, Y. W. Song, M. Zhao, X. Chen, Q. Zhang, J. Q. Huang, *Adv. Mater.* **2019**, *31*, 1903813.
- [64] F. Ma, Y. Wan, X. Wang, X. Wang, J. Liang, Z. Miao, T. Wang, C. Ma, G. Lu, J. Han, Y. Huang, Q. Li, *ACS Nano* **2020**, *14*, 10115–10126.
- [65] Y. Qiu, L. Fan, M. Wang, X. Yin, X. Wu, X. Sun, D. Tian, B. Guan, D. Tang, N. Zhang, *ACS Nano* **2020**, *14*, 16105–16113.
- [66] D. Guo, X. Zhang, M. Liu, Z. Yu, X. A. Chen, B. Yang, Z. Zhou, S. Wang, *Adv. Funct. Mater.* **2022**, 2204458.
- [67] Y. Li, T. Gao, D. Ni, Y. Zhou, M. Yousaf, Z. Guo, J. Zhou, P. Zhou, Q. Wang, S. Guo, *Adv. Mater.* **2022**, *34*, 2107638.
- [68] X. Meng, X. Liu, X. Fan, X. Chen, S. Chen, Y. Meng, M. Wang, J. Zhou, S. Hong, L. Zheng, G. Shi, C. W. Bielawski, J. Geng, *Adv. Sci.* **2022**, *9*, 2103773.
- [69] D. Luo, C. J. Li, Y. G. Zhang, Q. Y. Ma, C. Y. Ma, Y. H. Nie, M. Li, X. Weng, R. Huang, Y. Zhao, L. L. Shui, X. Wang, Z. W. Chen, *Adv. Mater.* **2022**, *34*, 2105541.
- [70] G. Zhao, Q. Chen, L. Wang, T. Yan, H. Li, C. Yuan, J. Mao, X. Feng, D. Sun, L. Zhang, *J. Mater. Chem. A* **2022**, *10*, 19893–19902.
- [71] J. Wang, W. Qiu, G. Li, J. Liu, D. Luo, Y. Zhang, Y. Zhao, G. Zhou, L. Shui, X. Wang, Z. Chen, *Energy Storage Mater.* **2022**, *46*, 269–277.
- [72] D. Fang, P. Sun, S. Huang, Y. Shang, X. Li, D. Yan, Y. V. Lim, C.-Y. Su, B.-J. Su, J.-Y. Juang, H. Y. Yang, *ACS Materials Lett.* **2021**, *4*, 1–10.
- [73] Y. Zhang, J. Liu, J. Wang, Y. Zhao, D. Luo, A. Yu, X. Wang, Z. Chen, *Angew. Chem. Int. Ed.* **2021**, *60*, 26622–26629; *Angew. Chem.* **2021**, *133*, 26826–26833.
- [74] S. Zhang, X. Ao, J. Huang, B. Wei, Y. Zhai, D. Zhai, W. Deng, C. Su, D. Wang, Y. Li, *Nano Lett.* **2021**, *21*, 9691–9698.
- [75] S. Zhang, Q. Shao, Y. Su, L. Xu, Q. Jiang, J. Chen, *J. Alloys Compd.* **2022**, *910*, 164799.
- [76] Y. Jia, W. Gong, X. Fan, S. Chen, X. Meng, Y. Meng, J. Zhou, Y. Cao, S. Hong, L. Zheng, Z. Wang, C. W. Bielawski, J. Geng, *Chem. Eng. J.* **2022**, *444*, 136546.
- [77] Y. Liu, Z. Wei, B. Zhong, H. Wang, L. Xia, T. Zhang, X. Duan, D. Jia, Y. Zhou, X. Huang, *Energy Storage Mater.* **2021**, *35*, 12–18.
- [78] P. Wang, B. Xi, Z. Zhang, M. Huang, J. Feng, S. Xiong, *Angew. Chem. Int. Ed.* **2021**, *60*, 15563–15571; *Angew. Chem.* **2021**, *133*, 15691–15699.
- [79] T. Huang, Y. Sun, J. Wu, Z. Shi, Y. Ding, M. Wang, C. Su, Y. Y. Li, J. Sun, *Adv. Funct. Mater.* **2022**, 2203902.
- [80] G. Liu, W. Wang, P. Zeng, C. Yuan, L. Wang, H. Li, H. Zhang, X. Sun, K. Dai, J. Mao, X. Li, L. Zhang, *Nano Lett.* **2022**, *22*, 6366–6374.
- [81] M. Chen, X. Zhao, Y. Li, P. Zeng, H. Liu, H. Yu, M. Wu, Z. Li, D. Shao, C. Miao, G. Chen, H. Shu, Y. Pei, X. Wang, *Chem. Eng. J.* **2020**, *385*, 123905.
- [82] S. Xie, X. Chen, C. Wang, Y. R. Lu, T. S. Chan, C. H. Chuang, J. Zhang, W. Yan, S. Jin, H. Jin, X. Wu, H. Ji, *Small* **2022**, *18*, 2200395.
- [83] J. Jin, Z. Sun, T. Yan, Z. Shi, M. Wang, T. Huang, Y. Ding, J. Cai, P. Wang, L. Zhang, J. Sun, *Small Sci.* **2022**, 2200059.
- [84] Y. Li, J. Wu, B. Zhang, W. Wang, G. Zhang, Z. W. Seh, N. Zhang, J. Sun, L. Huang, J. Jiang, J. Zhou, Y. Sun, *Energy Storage Mater.* **2020**, *30*, 250–259.
- [85] C. Lu, Y. Chen, Y. Yang, X. Chen, *Nano Lett.* **2020**, *20*, 5522–5530.
- [86] S. Yu, Y. Sun, L. Song, X. Cao, L. Chen, X. An, X. Liu, W. Cai, T. Yao, Y. Song, W. Zhang, *Nano Energy* **2021**, *89*, 106414.
- [87] R. Wang, R. Wu, X. Yan, D. Liu, P. Guo, W. Li, H. Pan, *Adv. Funct. Mater.* **2022**, *32*, 2200424.
- [88] W. Chen, H. Xia, K. Guo, W. Jin, Y. Du, W. Yan, G. Qu, J. Zhang, *Chem. Res. Chin. Univ.* **2022**, *38*, 1232–1238.
- [89] C. Zhao, G.-L. Xu, Z. Yu, L. Zhang, I. Hwang, Y.-X. Mo, Y. Ren, L. Cheng, C.-J. Sun, Y. Ren, X. Zuo, J.-T. Li, S.-G. Sun, K. Amine, T. Zhao, *Nat. Nanotechnol.* **2021**, *16*, 166–173.
- [90] C. Ma, Y. Zhang, Y. Feng, N. Wang, L. Zhou, C. Liang, L. Chen, Y. Lai, X. Ji, C. Yan, W. Wei, *Adv. Mater.* **2021**, *33*, 2100171.
- [91] X. Cao, M. Wang, Y. Li, L. Chen, L. Song, W. Cai, W. Zhang, Y. Song, *Adv. Sci.* **2022**, 202204027.
- [92] D. Zhang, S. Wang, R. Hu, J. Gu, Y. Cui, B. Li, W. Chen, C. Liu, J. Shang, S. Yang, *Adv. Funct. Mater.* **2020**, 2002471.
- [93] C. Zhou, M. Li, N. Hu, J. Yang, H. Li, J. Yan, P. Lei, Y. Zhuang, S. Guo, *Adv. Funct. Mater.* **2022**, 202204635.
- [94] J. Kim, S. J. Kim, E. Jung, D. H. Mok, V. K. Paidi, J. Lee, H. S. Lee, Y. Jeoun, W. Ko, H. Shin, B. H. Lee, S. Y. Kim, H. Kim, J. H. Kim, S. P. Cho, K. S. Lee, S. Back, S. H. Yu, Y. E. Sung, T. Hyeon, *Adv. Funct. Mater.* **2022**, 2110857.
- [95] Y. Ding, Q. Cheng, J. Wu, T. Yan, Z. Shi, M. Wang, D. Yang, P. Wang, L. Zhang, J. Sun, *Adv. Mater.* **2022**, *34*, 2202256.
- [96] R. Wang, R. Wu, C. Ding, Z. Chen, H. Xu, Y. Liu, J. Zhang, Y. Ha, B. Fei, H. Pan, *Nano-Micro Lett.* **2021**, *13*, 151.
- [97] X. Zhang, X. H. Liu, W. Zhang, Y. Z. Song, *Green Energy & Environ.* **2022**, DOI: 10.1016/j.gee.2022.03.006.
- [98] Y. Z. Song, H. Gao, M. L. Wang, L. Chen, X. Cao, L. X. Song, X. H. Liu, W. L. Cai, J. Y. Sun, W. Zhang, *EcoMat* **2022**, *4*, e12182.
- [99] R. Xiao, T. Yu, S. Yang, K. Chen, Z. Li, Z. Liu, T. Hu, G. Hu, J. Li, H.-M. Cheng, Z. Sun, F. Li, *Energy Storage Mater.* **2022**, *51*, 890–899.

Manuscript received: November 10, 2022

Revised manuscript received: December 14, 2022

Accepted manuscript online: December 14, 2022

Version of record online: January 5, 2023